

# Low-Loss Graded Dielectrics via Active Mixing of Nanocomposite Inks during 3D Printing

Bradley Duncan,\* Robert D. Weeks, Benjamin Barclay, Devon Beck, Patrick Bluem, Roberto Rojas, Maxwell Plaut, John Russo, Sebastien G. M. Uzel, Jennifer A. Lewis, and Theodore Fedynyshyn

Additive manufacturing has emerged as a promising approach for fabricating graded refractive index structures that control the electromagnetic response of radio frequency (RF) devices. However, current 3D printing methods cannot produce continuous gradients from multiple materials. Here, low-loss graded dielectrics via active mixing of nanocomposite inks composed of block copolymers and oxide nanoparticles are designed and printed. By simultaneously tailoring their rheological, printing, and their local filler particle-to-polymer ratio using an active mixing printhead, a conductive microstrip-graded substrate matching network with a gradually changing dielectric response, is created. In these printed devices, the impedance of the RF signal is controlled by the graded substrate rather than by varying the conductive microstrip geometry, enabling the fabrication of smaller RF devices. This approach enables the rapid design and fabrication of high-performance RF devices with locally tunable dielectric properties.

## 1. Introduction

The geometric design freedom enabled by emerging multi-material 3D printing techniques allows one to tailor materials composition and properties in a voxel-based manner.<sup>[1,2]</sup> Consequently, one can now fabricate more complex radio frequency (RF) devices that cannot be produced via traditional manufacturing methods, such as casting or molding.<sup>[3]</sup> Prior research has demonstrated this manufacturing versatility with a variety of RF structures such as frequency selective surfaces,<sup>[4]</sup>

antennas,<sup>[5]</sup> inductors,<sup>[6]</sup> and capacitors.<sup>[7]</sup> Graded index (GRIN) dielectrics in particular offer a promising route for creating RF components with reduced size, weight, and power that possess large frequency bandwidths.<sup>[8]</sup> The ability to fully control the electromagnetic properties of a dielectric substrate via 3D printing provides additional degrees of design freedom for miniaturizing GRIN RF lenses, high-performance superstrates for phased arrays, and obfuscated electronic systems.

Most graded dielectrics are patterned by placing air voids within a printed structure<sup>[9]</sup> or spatially patterning two distinct dielectric materials within the same part.<sup>[10]</sup> Space filling methods that vary the amount of air and dielectric material at the voxel level generate architected devices, such as a Luneburg lenses, that can effectively focus RF radiation.<sup>[11]</sup> However, these highly porous architectures are not mechanically robust, limiting their utility in constrained platforms, such as unmanned aerial vehicles<sup>[12]</sup> or small satellites.<sup>[13]</sup> Multimaterial 3D printing can be used to print dense GRIN devices with discrete blocks of varying dielectric materials. Polymer nanocomposites are often used, because they provide a wide range of electromagnetic properties compared to pure polymers.<sup>[14,15]</sup> For example, Isakov et al. demonstrated the printing of a flat GRIN lens by depositing varying amounts of high and low relative permittivity materials in adjacent sections.<sup>[10]</sup> These printed blocks generate RF structures in which the relative permittivity depends on both the volumetric combination of the different dielectric materials used and the operating frequency of the device. However, these discretely graded structures possess sharp interfaces between disparate materials, which can lead to mismatches in thermal expansion coefficients and limit device performance. The ability to produce continuously graded architectures would accelerate the development of next-generation RF systems.

Here, we report the fabrication of continuously graded dielectric RF devices via 3D printing of nanocomposite inks using an active mixing nozzle.<sup>[16]</sup> Our direct ink writing method allows for compositional and geometric control over architected dielectrics. We describe and characterize a wide range of printed composites whose relative permittivity is engineered by varying the polymer-to-nanoparticle filler ratio on-the-fly during 3D printing. Continuously graded architectures that lack abrupt

B. Duncan, B. Barclay, D. Beck, P. Bluem, R. Rojas, M. Plaut, J. Russo, T. Fedynyshyn  
MIT Lincoln Laboratory  
Lexington, MA 02420, USA  
E-mail: bradley.duncan@ll.mit.edu

R. D. Weeks, S. G. M. Uzel, J. A. Lewis  
Harvard School of Engineering and Applied Science and Wyss Institute for Biologically Inspired Engineering  
Cambridge, MA 02138, USA

 The ORCID identification number(s) for the author(s) of this article can be found under <https://doi.org/10.1002/admt.202201496>.

© 2022 The Authors. Advanced Materials Technologies published by Wiley-VCH GmbH. This is an open access article under the terms of the Creative Commons Attribution License, which permits use, distribution and reproduction in any medium, provided the original work is properly cited.

DOI: 10.1002/admt.202201496

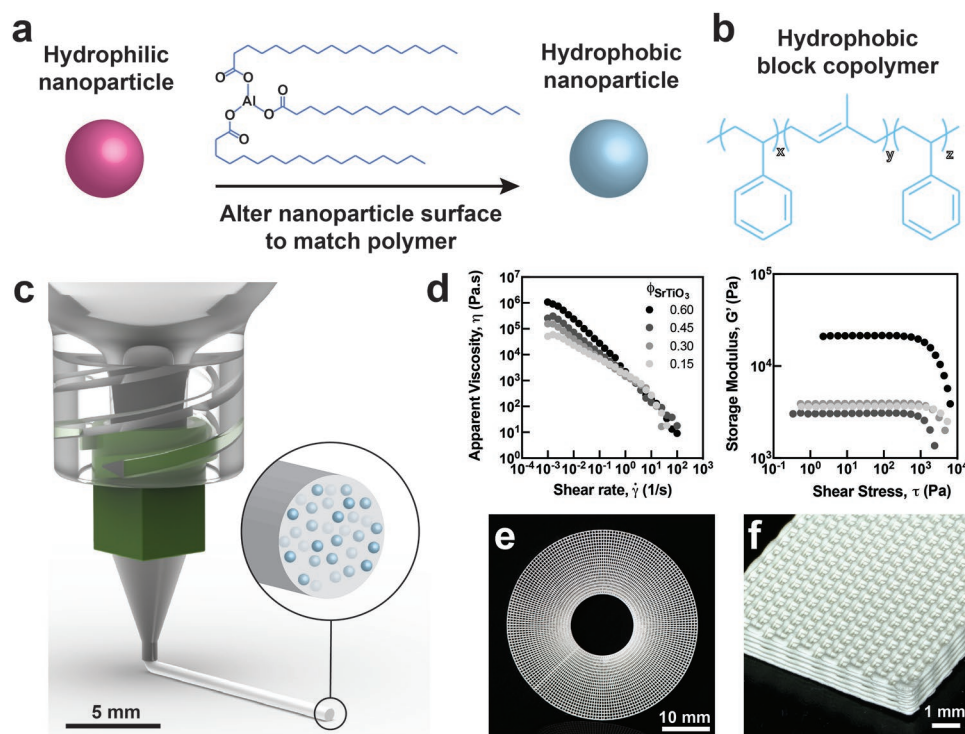


**Figure 1.** Low-loss dielectric composites via 3D printing of nanocomposite inks. a) Synthetic scheme used to modify the surface of the oxide nanoparticles. b) Molecular structure of the triblock copolymer matrix used in these inks. c) Schematic illustration of a printed filament composed of a nanocomposite ink. d) Apparent viscosity as a function of shear rate (left) and storage modulus as a function of shear stress (right) for triblock copolymer inks filled with varying volume fraction ( $\phi$ ) of SrTiO<sub>3</sub> nanoparticles. e) Optical image of a printed radial lattice composed of a triblock copolymer ink filled with TiO<sub>2</sub> nanoparticles ( $\phi = 0.30$ ). f) Optical image of a printed simple cubic lattice composed of a triblock copolymer ink filled with SrTiO<sub>3</sub> nanoparticles ( $\phi = 0.45$ ).

material interfaces are produced and characterized in the form of microstrip line devices to demonstrate these capabilities.

## 2. Results and Discussion

Styrenic triblock copolymers are a versatile matrix for generating low-loss, 3D printable structures.<sup>[17]</sup> The addition of nanoparticle-based oxide fillers offers a viable path for increasing the relative permittivity,  $\epsilon_r$ , of the printed structures.<sup>[16]</sup> Building on this prior work, we created printable nanocomposite inks composed of surface-modified oxide nanoparticles rendered compatible with a low-loss polymer matrix. Specifically, aluminum stearate is used to alter the hydrophilic surface of Al<sub>2</sub>O<sub>3</sub> ( $\epsilon = 10 @ 34$  GHz), TiO<sub>2</sub> ( $\epsilon = 50 @ 34$  GHz), and SrTiO<sub>3</sub> ( $\epsilon = 300 @ 34$  GHz) nanoparticles (Figure 1a) of varying dielectric constant.<sup>[18]</sup> Multiple characterization methods are used to confirm their successful surface modification (Figures S1 and S2; Table S1, Supporting Information). The modified nanoparticles are then combined with a hydrophobic styrene–isoprene–styrene (SIS) triblock copolymer, whose structure is shown in Figure 1b. Printable nanocomposite inks are formulated from three constituents: surface-functionalized nanoparticles, SIS, and toluene. These inks can be actively mixed and printed as filaments to create architected dielectrics for RF applications, as shown in Figure 1c. By contrast, traditional casting and molding techniques typically yield monolithic dielectric substrates.

Our nanocomposite inks are designed to exhibit the requisite viscoelastic response for direct writing, that is, they flow through the nozzle once a critical pressure is reached, yet rapidly solidify upon exiting the nozzle to retain their printed shape. Prior work has shown that concentrated solutions of styrenic block copolymers in aromatic solvents exhibit shear thinning properties.<sup>[19,20]</sup> Their strong shear thinning behavior reduces the printing pressure required, as shown for a representative SIS-based ink with varying SrTiO<sub>3</sub> volume fraction (Figure 1d). A summary of the low-shear apparent viscosity for inks with each filler type and varying filler volume fraction,  $\phi$ , is provided in Table S2, Supporting Information. We have defined the shear yield stress,  $\tau_y$ , as the shear stress at which the storage modulus,  $G'_{\max}$ , is 90% of its plateau value, which corresponds to the onset of yielding.<sup>[17]</sup> The respective  $G'_{\max}$  values for these composites are  $3.6 \times 10^3$  Pa ( $\phi = 0.15$ ),  $3.9 \times 10^3$  Pa ( $\phi = 0.30$ ),  $3.1 \times 10^3$  Pa ( $\phi = 0.45$ ), and  $21.3 \times 10^3$  Pa ( $\phi = 0.60$ ). Upon yielding, there is a pronounced decrease in  $G'$  for SIS-SrTiO<sub>3</sub> inks with varying filler volume fractions (Figure 1d), which occurs when the applied stress exceeds their shear yield stress ( $\tau_y$ ) values of  $2.3 \times 10^3$  Pa ( $\phi = 0.15$ ),  $1.4 \times 10^3$  Pa ( $\phi = 0.30$ ),  $8.4 \times 10^2$  Pa ( $\phi = 0.45$ ), and  $8.5 \times 10^2$  Pa ( $\phi = 0.60$ ). Their relatively high shear elastic modulus in the quiescent state ( $\tau = 0$ ) enables the printed filaments to keep their filamentary shape, even as subsequent layers are printed in the form of 3D lattices (Figure 1e,f). For each nanocomposite ink,  $\tau_y$  decreases as the nanoparticle filler volume fraction increases.

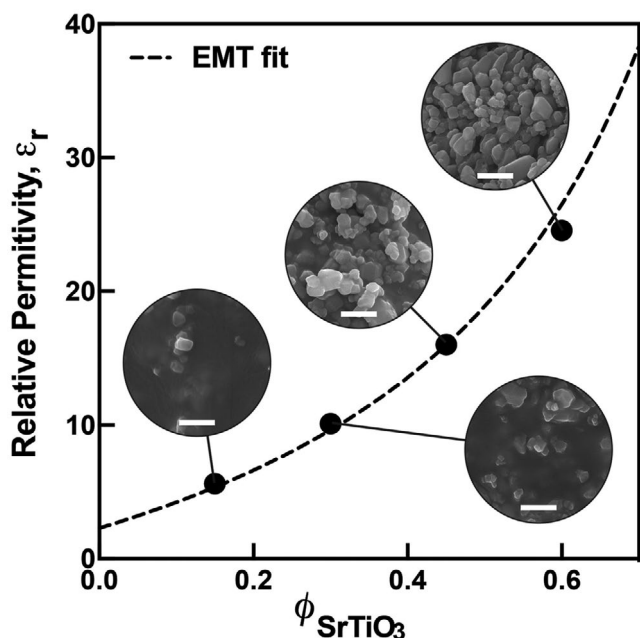


**Figure 2.** Relative permittivity as a function of SrTiO<sub>3</sub> nanoparticle volume fraction for composite dielectrics inks. Corresponding SEM images of these inks at specific filler volume fractions. Scale bars = 0.5 μm. (Note: Dashed line denotes the relative permittivity predicted by effective medium theory over this compositional range.)

We next printed dielectric samples from the nanocomposite inks listed in Table S2, Supporting Information, and characterized their relative permittivity and loss tangent (Table S4, Supporting Information). As expected, both properties increase with increasing filler volume fraction, which can be modeled using an effective medium theory (EMT) model (Figure 2). Equation (1), derived from Bruggeman theory, is used for this model.<sup>[21]</sup>

$$\epsilon = \epsilon_B \left[ 1 + \frac{\phi_A (\epsilon_A - \epsilon_B)}{\epsilon_B + n(1 - \phi_A)(\epsilon_A - \epsilon_B)} \right] \quad (1)$$

Three dependent variables comprise the EMT model,  $\phi_A$  is the oxide nanoparticle volume fraction, and  $\epsilon_A$  and  $\epsilon_B$  are the relative permittivity values of the filler particle and SIS, respectively. The relative permittivity of the printed nanocomposite is represented by  $\epsilon$ . Data points at a  $\phi = 0$  (unfilled ink) correspond to measurements for pure SIS. This model utilizes one fitted parameter,  $n$ , as the ceramic morphology factor. Non-linear regression was used to fit the model to five experimental data points for each filler type. The value of  $n$  was determined to be 0.46, 0.18, and 0.12 for Al<sub>2</sub>O<sub>3</sub>, TiO<sub>2</sub>, and SrTiO<sub>3</sub> nanoparticles, respectively. These values are in good agreement with other nanocomposite systems.<sup>[22]</sup> Figure 2 also shows scanning electron microscopy (SEM) images of the cross-sections of printed SIS-SrTiO<sub>3</sub> filaments as a function of varying filler volume fraction.

Graded dielectrics offer significant advantages for producing high-performance RF devices.<sup>[10,23,24]</sup> To fabricate these devices, we implemented 3D multimaterial printing coupled with an active mixing printhead that enables the composition of viscoelastic inks to be altered on-the-fly.<sup>[16,25]</sup> We custom

designed and built an active mixing nozzle, which is integrated with our 3-axis motion-controlled printing stage (Figure 3a,b). Two inlet streams from reservoirs containing pure and nanocomposite inks are actively mixed (Tables S2 and S3, Supporting Information) using two volumetric dispensing pumps that are connected directly to the printer's controller. The ratio of these two inks in the mixing chamber is synchronized with the motion of the printer, while a rotating impeller is used to mix these inks upon entry into the chamber from each inlet. A homogeneous filament is then extruded from the nozzle (686 μm in diameter). The length of the mixing chamber is 21.6 mm which is two orders of magnitude longer than the calculated minimum length needed, based on the model developed by Ober et al.,<sup>[16]</sup> to achieve efficient mixing of non-Brownian particles for the geometry and operating parameters of our system. Overall, this method enables architected RF devices with relative permittivity values ranging from 2.2 to 24.5 to be printed in a continuously graded fashion without sharp transitions between the two inks.

The dead volume of the mixing chamber introduces an offset between what is commanded to the volumetric extruders and what is extruded at the nozzle end. A meander produced from switching between two inks (unfilled and filled) results in gradients that can require additional material to be extruded to produce parts that match the designed gradient (Figure 3c). Additionally, since the meander is split into discrete filaments, the resulting composition changes in a stepwise fashion unlike the smooth continuous targeted composition (Figure 3d). To characterize the performance of our active mixing printhead, we designed a model structure to determine how much material must be printed to transition from the unfilled to filled ink formulation. The meander was printed by first injecting the pure SIS ink into the mixing chamber. After a programmed distance, injection of this ink was halted and the SIS-SrTiO<sub>3</sub> ( $\phi = 0.6$ ) ink was injected to the mixing chamber. Representative sections from the printed meander, shown in Figure 3e, were cut and their polymer content was then measured by thermogravimetric analysis (TGA). Figure 3f shows both the initial delay of 120 mm between the command and a compositional change, followed by an exponential decay when switching materials. Our active mixing printhead contains an internal volume of ≈0.13 mL, which translates to a minimum of ≈344 mm of extruded filament to fully switch between these two composition extremes using the 686 μm diameter nozzle. Based on the TGA results, we observed that 740 mm of extrusion from the 686 μm diameter nozzle (0.27 mL) is required for the switch to achieve 99% SIS-SrTiO<sub>3</sub> ( $\phi = 0.6$ ) ink. We account for this switching volume in the printing codes used for subsequent RF designs. We anticipate a marked reduction in this switch-over distance could be achieved by reducing the volume of the mixing chamber and altering the physiochemical properties of the mixing chamber walls.<sup>[16]</sup>

To demonstrate the versatility of our approach, we designed two wideband matching networks. The first matching network is designed using the traditional approach of a uniform dielectric substrate where the geometry of the conductive trace is used to dictate the RF behavior of the device. By contrast, the second matching network consists of a uniform conductive trace geometry with a graded dielectric substrate to control the

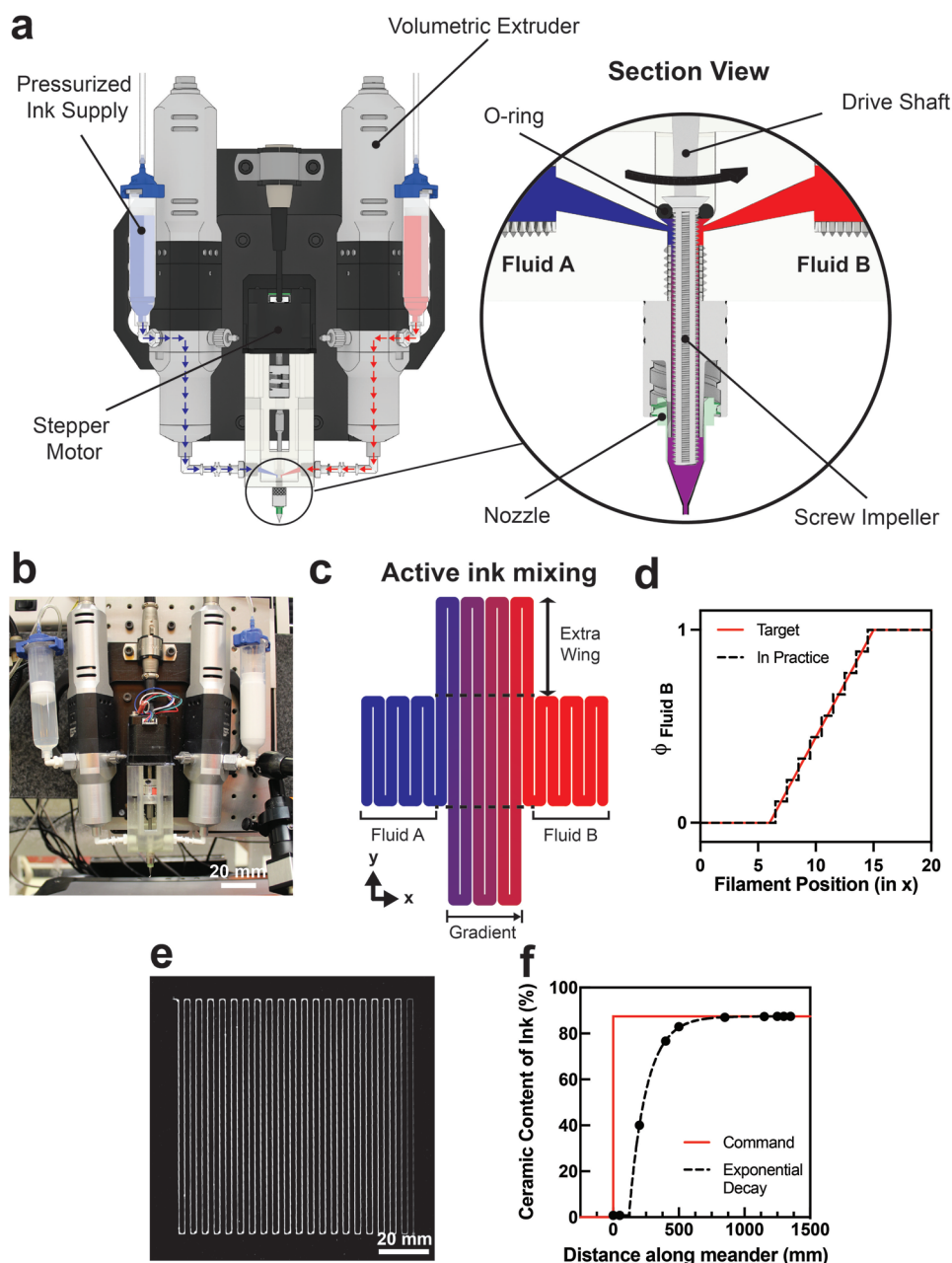


**Figure 3.** Active mixing during 3D printing. a) Schematic of the fluid path and important components of the mixing nozzle. b) Photograph of custom active mixing nozzle used in this study. Clear SIS ink is fed into the mixing chamber from the left side and the white SrTiO<sub>3</sub> ink is fed into the mixing chamber from right side. c) Schematic of printed gradient transitioning from fluid A to B. The extra wing sections are added to part designs to account for the switch over volume of the mixing chamber. d) Comparison between the idealized smooth gradient target and the resulting step-like gradient achieved with a meander. e) Photograph of a printed meander used to determine the offset volume. f) Plot depicting the distance required to fully change the composition of the extruded filament from one ink to the other.

RF performance. The function of these devices is to impedance match a standard transmission line (characteristic impedance of 50  $\Omega$ ) to a 20  $\Omega$  load over a large frequency bandwidth (10–40 GHz). Notably, both devices are designed to provide similar RF behavior, yet achieved through vastly different electromagnetic interactions. The traditional method to achieve a large bandwidth matching network is to use a tapered transmission line. We designed a matching network as shown in **Figure 4a**

where the characteristic impedance of the microstrip transmission line decreases from 50  $\Omega$  at the narrower line width to 20  $\Omega$  at the wider line width. To determine the optimum taper geometry, we used a Klopfenstein impedance taper<sup>[26]</sup> as it yields the lowest reflection coefficient over the frequency band of interest. The width of the tapered line for this example can be expressed by a polynomial as shown in Equation (2) where  $x$  is the principal axis of the transmission line.

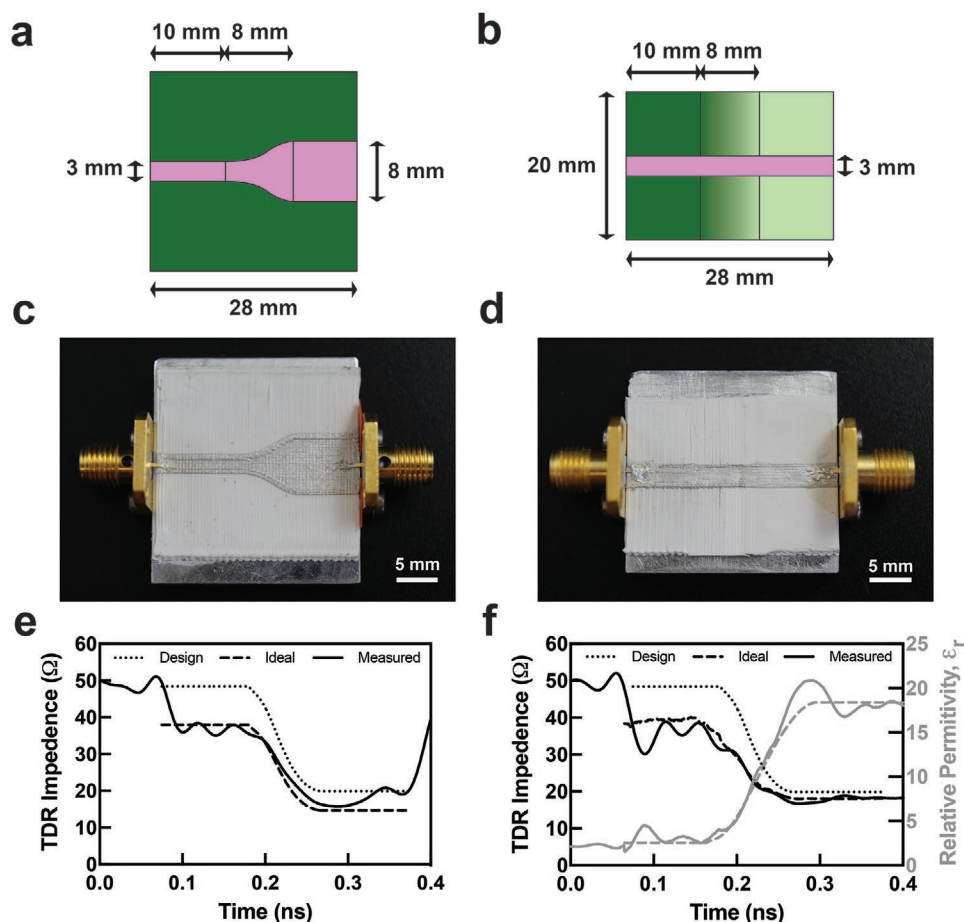


**Figure 4.** Printed RF Devices. a) Schematic view of Klopfenstein taper transmission line design. b) Schematic view of GRIN transmission line design with the lighter green corresponding to an increasing relative permittivity. c) Image of printed Klopfenstein taper transmission line. d) Image of printed GRIN transmission line. e) Plot of the time domain reflectometry measurements of the printed Klopfenstein taper. f) Plot of the time domain reflectometry measurements of the printed GRIN substrate.

$$y = \pm(Ax^5 + Bx^4 + Cx^3 + Dx^2 + Ex + F) \quad \text{for } 0 \leq x \leq 8 \text{ mm} \quad (2)$$

$$A = 5.604 \times 10^{-4}, B = -0.0141, C = 0.1020, D = -0.1418 \\ E = 0.2851, F = 2.662$$

The +/- signs refer to the top and bottom edges of the tapered line as measured from the center of transmission line. The device was designed with a substrate thickness of 1 mm and a uniform relative permittivity of 3. By harnessing a GRIN substrate, the same matching network can be designed with a transmission line of constant width. Instead of tapering the width of transmission line, the relative permittivity of the substrate was varied along the X-direction (axis of transmission line) as shown in Figure 4b. The width of the transmission line was designed as 3.175 mm and the thickness of the substrate as 1 mm. However, the relative permittivity of the middle portion of the substrate was designed to follow Equation (3). This relative permittivity profile of the GRIN substrate produces the same electromagnetic behavior as the Klopfenstein taper line.<sup>[27]</sup> Broadly, this GRIN approach takes traditional geometric RF design rules and augments these principles by introducing an additional degree of freedom within the composition of the substrate in three dimensions.

$$\varepsilon = Ax^4 + Bx^3 + Cx^2 + Dx + E \quad \text{for } 0 \leq x \leq 8 \text{ mm} \quad (3)$$

$$A = -0.01402, B = 0.1751 \\ C = -0.3261, D = 0.562 \\ E = 2.539$$

Methods for measuring GRIN materials at microwave frequencies have not been well explored. We used time domain reflectometry to characterize our printed parts, as this technique measures the amount of transmitted and reflected signals over time on the input and output of the network which correspond to physical, and therefore, electrical variations in the network. The method shown here leverages the time domain signal and extends it to defining the transmission line characteristic impedance over propagation time. By analyzing the impedance behavior over time and accurately measuring the physical parameters of the circuit, the material parameters of the substrate can be extracted and interpreted over the length of the circuit. The printed traditional Klopfenstein taper is shown in Figure 4c and the printed GRIN substrate is shown in Figure 4d. The conductive traces were printed using an SIS-silver flake ink composite ink as described in Table S2, Supporting Information. Although the substrates were designed for a thickness of 1 mm, due to the geometry of the printing

nozzle, the average measured thickness for the substrate of the Klopfenstein taper was measured to be 0.7 mm. The GRIN substrate's height varied from around 0.7 mm at the left port to 1 mm at the right port. The average value as well as the variable substrate thickness were used to recalculate the characteristic impedances of the matching networks and they are labeled as "Ideal" in Figure 4e,f. Figure 4e shows the measured characteristic impedance of the standard microwave matching network (Figure 4c) where the actual matching network corresponds to the time from around 0.19 to around 0.25 ns. In this region, the agreement between measured and ideal values is very good. The region 0.1 to around 0.19 ns corresponds to the constant width transmission line region where the measured characteristic impedance oscillates around  $40 \Omega$ . In the region 0 to 0.1 ns the characteristic impedance oscillates around  $50 \Omega$  because that region corresponds to the SMA connector. The region 0.25 to 0.35 ns corresponds to the constant width region near the 2nd port. Finally, the region larger than 0.35 ns corresponds to the transition to the SMA connector in the 2nd port. Good agreement is also shown between the ideal and measured GRIN dielectric profile in Figure 4f where the measured relative permittivity of the GRIN substrate (0.19 to 0.28 ns) varies from around 2.5 to 18. The regions 0.07 to 0.19 and 0.28 to 0.38 ns correspond to substrates of uniform relative permittivity of 2.5 and 18, respectively.

### 3. Conclusions

In summary, we have developed a generalized strategy to fabricate graded RF devices. By combining functionalized ceramic fillers with low-loss triblock copolymers, we have shown that dielectric materials with relative permittivity values ranging from 2.2–24.5 can be printed. Notably, our direct ink writing approach can generate graded dielectric structures which cannot be built using other manufacturing techniques. This capability offers an alternative method to traditional geometric-based approaches for impedance matching transmission lines. More broadly, this plug-and-play materials suite coupled with active mixing-based, 3D printing allows one to deterministically define the geometry and composition of printed devices. These capabilities are expected to accelerate the development of GRIN RF lenses, high-performance superstrates for phased arrays, and obfuscated electronic systems.

### 4. Experimental Section

**Materials:** Polystyrene-block-polyisoprene-block-polystyrene (SIS) (432415) was acquired from Sigma-Aldrich, St. Louis, MO. Toluene (9466-03) was acquired from Avantor, Center Valley, PA. Bare TiO<sub>2</sub> rutile nanoparticles (US3535) and Al<sub>2</sub>O<sub>3</sub> alpha nanoparticles (US3008) were purchased from US Research Nanomaterials, Inc., Houston, TX. SrTiO<sub>3</sub> nanoparticles were purchased from TPL Inc. Aluminum stearate (130815) was acquired from Beantown Chemical, Hudson, NH. Silver flakes (47MR-10F) were purchased from Inframat. 3 and 30 mL luer-lock polypropylene syringes and an HP 7× high pressure adapter were purchased from Nordson EFD, Westlake, OH.

**Surface Modification of Oxide Nanoparticles:** Particles were modified by combining 500 mL of toluene, 50 g of the bare nanoparticles, and 2.5 g of aluminum stearate in a 1000 mL round bottom flask. The reactions were

heated to reflux, and a Dean–Stark trap was used to remove water from the reactions. The refluxing reactions were stirred for 48 h. The reactions were then allowed to cool to room temperature and the particles were purified using centrifugation. Reaction contents were transferred and centrifuged at 9000 RPM for 10 min. The clear supernatant was poured off. The particles were suspended and centrifuged again in toluene (2×) and methanol (1×) to remove excess ligands. The purified nanoparticles were dried under vacuum for 48 h. The functionalized nanoparticles were filtered through a No. 230 (63 μm) Hogentogler sieve (5214) to remove larger aggregates prior to use.

**Ink Formulation:** Printable inks were created by combining polymer with an aromatic solvent in a Speedmixer DAC 600.2 Vac-LR planetary mixer (Flacktek, Landrum SC) and mixed at 2000 RPM for 5 min. Filler particles were then added to the mixing container and spun following a mixing cycle of 30 s at 800 RPM, 30 s at 1200 RPM, and 2 min at 2000 RPM. This cycle was repeated until a homogeneous ink was obtained.

**Attenuated Total Reflectance FTIR:** Analyses were performed on a Bruker Vertex 70 FTIR spectrophotometer fitted with a Platinum Attenuated Total Reflectance QuickSnap sampling module. The nanoparticles and reagents were analyzed as neat solids.

**Rheology Measurements:** Inks were characterized by a DHR-2 Rheometer (TA Instruments, New Castle, DE) using a 20 mm cone-and-plate geometry.

**Printing:** For single material printing, inks were loaded into 3 mL luer-lock polypropylene syringes, capped on top and bottom, and centrifuged at 1000 RPM for 15 min to remove air bubbles and force ink to the bottom of the syringe barrel. The syringe was uncapped, loaded into an HP 7× high-pressure adapter, and mounted to a 3-axis Aerotech (Pittsburgh, PA) gantry system. Ink was extruded through a 233 μm, S-Type, luer-lock tapered nozzle using house air through an Ultimius V pressure control box (Nordson EFD). For printing with the active mixing nozzle, inks were loaded into 30 mL luer-lock polypropylene syringes, capped on top and bottom, and centrifuged at 1000 RPM for 15 min to remove air bubbles and force ink to the bottom of the syringe barrel. The syringes were uncapped, attached to the vipro-HEAD 3 volumetric dispersers (ViscoTec), and the printhead was mounted to a 3-axis Aerotech (Pittsburgh, PA) gantry system. Inks were held at a constant pressure of 40 PSI during printing. The mixing impeller was rotated at a constant rate of 300 RPM during printing to ensure complete mixing of the inks. Ink was extruded through a 686 μm, S-Type, luer-lock tapered nozzle (GPD Global). Parts were left to dry at room temperature for 24 h prior to removal from the build plate to ensure complete evaporation of the solvent.

**Thermogravimetric Analysis:** The oxide filler content within graded dielectrics produced by 3D printing was determined using a TA Instruments Q50 TGA ran in the presence of oxygen. ≈10 mg of coated particle sample was weighed out onto the pan for each run. The program procedure consisted of a 10 °C min<sup>-1</sup> ramp to 100 °C, isotherm for 30 min at 100 °C, and then a final ramp of 10 °C min<sup>-1</sup> to 600 °C. Mass losses were measured as the percent change in mass from 125 to 600 °C.

**Dielectric Property Measurements:** Complex dielectric permittivity was measured using a rectangular waveguide and a Keysight E8364C Vector Network Analyzer. Printed or melt-cast slabs of dielectric between one-half and a few wavelengths were placed inside a 2 in. length of split-block waveguide or loaded into 0.050" waveguide shims (L3 Harris Narda-ATM, Hauppauge, NY). Measurements were made in the Ka band (26.5 to 40 GHz). Relative permittivity and loss values were taken as the median value across the Ka band.

**Scanning Electron Microscopy:** Images were taken using a Zeiss LEO 1525 field emission scanning electron microscope. Samples were coated in chromium before loading to reduce charging. The electron beam was created at 1 kV and a secondary electron detector was used to construct the image.

**GRIN Device Measurements:** Dielectric substrates were printed onto a PTFE sheet using the active mixing nozzle. Conductive traces were subsequently printed onto the dielectric substrate. Parts were then cut to exact dimensions with a razor blade and mounted onto a ¼" thick

aluminum substrates. SMA connectors (A99392-ND, Digi-Key, Thief River Falls MN) were attached to the aluminum substrates and pins were electrical connected to the printed traces using a small amount of the SIS-silver flake ink. Scattering parameters were measured from 10 MHz to 26 GHz using a Rohde & Schwarz ZVA50 Vector Network Analyzer. Relative permittivity data were extracted from the scattering parameter data using the physical height of the substrate and the width of the transmission line as a basis for the time domain extraction. Results were smoothed using a hamming window to reduce high frequency content in the Fourier transform.

## Supporting Information

Supporting Information is available from the Wiley Online Library or from the author.

## Acknowledgements

The authors thank David Scott for his assistance in fabricating components for the mixing nozzle. This material is based upon the work supported by the Assistant Secretary of Defense for Research and Engineering under Air Force Contract No. FA8721-05-C-0002 and/or FA8702-15-D-0001. Any opinions, findings, conclusions, or recommendations expressed in this material are those of the author(s) and do not necessarily reflect the views of the Assistant Secretary of Defense for Research and Engineering. J.A.L. and R.D.W. gratefully acknowledge support provided from the NSF through the Designing Materials to Revolutionize and Engineer our Future (DMREF) Award number DMR-1922321 and from the United States Air Force under Contract No. FA8650-16-D-5851, through a subcontract from the UES No. S-124-020-001.

## Conflict of Interest

The authors declare no conflict of interest.

## Data Availability Statement

The data that support the findings of this study are available from the corresponding author upon reasonable request.

## Keywords

3D printing, dielectrics, graded index, nanocomposites

Received: September 9, 2022

Revised: October 12, 2022

Published online:

- [1] M. A. Skylar-Scott, J. Mueller, C. W. Visser, J. A. Lewis, *Nature* **2019**, 575, 330.
- [2] J. Hiller, H. Lipson, *Rapid Prototyping J.* **2009**, 15, 137.
- [3] A. Bandyopadhyay, B. Heer, *Mater. Sci. Eng., R* **2018**, 129, 1.
- [4] S. A. Nauroze, L. S. Novelino, M. M. Tentzeris, G. H. Paulino, *Proc. Natl. Acad. Sci. USA* **2018**, 115, 13210.
- [5] K. J. Byers, C. Barr, *IEEE Antennas Wirel. Propag. Lett.* **2018**, 17, 5.
- [6] R. A. Ramirez, E. A. Rojas-Nastrucci, T. M. Weller, *IEEE Trans. Microwave Theory Tech.* **2018**, 66, 5462.
- [7] M. T. Craton, X. Konstantinou, J. D. Albrecht, P. Chahal, J. Papapolymerou, *IEEE Trans. Microwave Theory Tech.* **2020**, 68, 3418.
- [8] J. B. Pendry, *Science* **2006**, 312, 1780.
- [9] Y.-H. Lou, Y.-X. Zhu, G.-F. Fan, W. Lei, W.-Z. Lu, X.-C. Wang, *IEEE Antennas Wirel. Propag. Lett.* **2021**, 20, 234.
- [10] D. Isakov, C. J. Stevens, F. Castles, P. S. Grant, *Adv. Mater. Technol.* **2016**, 1, 1600072.
- [11] M. Liang, W.-R. Ng, K. Chang, K. Gbele, M. E. Gehm, H. Xin, *IEEE Trans. Antennas Propag.* **2014**, 62, 1799.
- [12] T. Lampersberger, R. Feger, A. Haderer, C. Egger, M. Friedl, A. Stelzer, in *2018 15th European Radar Conf. (EuRAD)*, **2018**, pp. 393–396, <https://doi.org/10.23919/EuRAD.2018.8546529>.
- [13] A. Kwas, E. MacDonald, C. J. Kief, R. Wicker, C. Soto, L. Bañuelos, J. Aarestad, B. Zufelt, J. D. Stegeman, C. Tolbert, in *AIAA SPACE 2014 Conference and Exposition*, American Institute of Aeronautics And Astronautics, San Diego, CA **2014**.
- [14] F. Castles, D. Isakov, A. Lui, Q. Lei, C. E. J. Dancer, Y. Wang, J. M. Janurudin, S. C. Speller, C. R. M. Grovenor, P. S. Grant, *Sci. Rep.* **2016**, 6, 22714.
- [15] M. Haghzadeh, C. Armiento, A. Akyurtlu, *IEEE Trans. Microw. Theory Techn.* **2017**, 65, 2030.
- [16] T. J. Ober, D. Foresti, J. A. Lewis, *Proc. Natl. Acad. Sci. USA* **2015**, 112, 12293.
- [17] M. Lis, M. Plaut, A. Zai, D. Cipolle, J. Russo, J. Lewis, T. Fedynyshyn, *Adv. Mater. Technol.* **2016**, 1, 1600027.
- [18] T. A. Egerton, N. J. Everall, I. R. Tooley, *Langmuir* **2005**, 21, 3172.
- [19] G. Kraus, J. T. Gruver, *J. Appl. Polym. Sci.* **1967**, 11, 2121.
- [20] D. R. Paul, J. E. St. Lawrence, J. H. Troell, *Polym. Eng. Sci.* **1970**, 10, 70.
- [21] Y. Rao, J. Qu, T. Marinis, C. P. Wong, *IEEE Trans. Compon. Packag. Technol.* **2000**, 23, 434.
- [22] H. Wang, H. Yang, J. Tong, Q. Zhang, *J. Appl. Polym. Sci.* **2019**, 136, 47980.
- [23] Z. Larimore, S. Jensen, P. Parsons, B. Good, K. Smith, M. Mirotnik, *Addit. Manuf.* **2017**, 15, 48.
- [24] J. Yi, G.-P. Piau, A. de Lustrac, S. N. Burokur, *Sci. Rep.* **2016**, 6, 30661.
- [25] J. M. Ortega, M. Golobic, J. D. Sain, J. M. Lenhardt, A. S. Wu, S. E. Fisher, L. X. P. Perez, A. W. Jaycox, J. E. Smay, E. B. Duoss, T. S. Wilson, *Adv. Mater. Technol.* **2019**, 4, 1800717.
- [26] R. E. Collin, *Foundations for Microwave Engineering*, IEEE Press, New York **2001**.
- [27] D. M. Pozar, *Microwave Engineering*, 4th ed., Wiley, Hoboken, NJ **2012**.